



# Increased ocean heat transport into the Nordic Seas and Arctic Ocean over the period 1993–2016

Takamasa Tsubouchi<sup>1</sup>✉, Kjetil Våge<sup>1</sup>, Bogi Hansen<sup>2</sup>, Karin Margretha H. Larsen<sup>2</sup>, Svein Østerhus<sup>3</sup>, Clare Johnson<sup>4</sup>, Steingrímur Jónsson<sup>5,6</sup> and Héðinn Valdimarsson<sup>6</sup>

**Warm water of subtropical origin flows northward in the Atlantic Ocean and transports heat to high latitudes. This poleward heat transport has been implicated as one possible cause of the declining sea-ice extent and increasing ocean temperatures across the Nordic Seas and the Arctic Ocean, but robust estimates are still lacking. Here, we use a box inverse model and more than 20 years of volume transport measurements to show that the mean ocean heat transport was  $305 \pm 26$  TW for 1993–2016. A significant increase of 21 TW occurred after 2001, which is sufficient to account for the recent accumulation of heat in the northern seas. Ocean heat transport may therefore have been a major contributor to climate change since the late 1990s. This increased heat transport contrasts with the Atlantic Meridional Overturning Circulation (AMOC) slowdown at mid-latitudes and indicates a discontinuity of the overturning circulation measured at different latitudes in the Atlantic Ocean.**

The Atlantic Meridional Overturning Circulation (AMOC) is the large-scale, bidirectional circulation in the Atlantic Ocean that transports warm subtropical-origin Atlantic water (AW) northward near the surface and cold, dense water southward at depth, connected by warm-to-cold water mass transformation at high latitudes<sup>1</sup>. Most of the AW enters the Norwegian Sea between Iceland and Scotland (Fig. 1a). The volume and temperature of the AW transported into the Nordic Seas exert a strong influence on climate in northern Europe<sup>2,3</sup>. As the warm water progresses northward toward the Arctic Ocean, heat is continually released to the atmosphere and the AW becomes colder and denser. Before reaching Fram Strait between Greenland and the Svalbard archipelago, the AW has attained sufficient density to supply the dense overflow water (OW) plumes that pass through gaps in the Greenland–Scotland Ridge (GSR) and form the headwaters to the lower limb of the AMOC<sup>4</sup>. Some additional transformation also takes place in the Barents Sea<sup>5</sup> and Arctic Ocean<sup>6</sup>. Recent observational programmes emphasize the importance of this warm-to-cold water mass transformation in the Nordic Seas and Arctic Ocean (jointly referred to as the Arctic Mediterranean) to the AMOC<sup>7,8</sup>.

The Arctic Mediterranean has accumulated heat over the last decades as manifested by increased ocean heat content and reduced sea ice volume<sup>9–12</sup>. The Norwegian Sea experienced warming at a rate of  $3.2 \text{ W m}^{-2}$  during 1995–2010 (ref. <sup>9</sup>) and approximately  $7 \text{ W m}^{-2}$  during 2011–2018 (ref. <sup>10</sup>). Long-term hydrographic monitoring has documented a widespread increase in upper ocean temperature along AW pathways from the Rockall Trough to Fram Strait since 2000 (refs. <sup>13–15</sup>). At higher latitudes, the Eurasian Basin of the Arctic Ocean and, in particular, the northern Barents Sea are going through a marine climate transition referred to as ‘Atlantification’, which is associated with enhanced surface presence of AW, reduced sea ice cover, a weakened halocline and deeper wintertime convection<sup>16–18</sup>. Despite a dearth of hydrographic observations in the Arctic Ocean, recent studies relying on data assimilation demonstrated that north of  $70^\circ \text{N}$  heat has accumulated at a rate of  $\sim 1 \text{ W m}^{-2}$  (equivalent to  $\sim 12 \text{ TW}$  over the entire region north of  $70^\circ \text{N}$ ) since 2000 (refs. <sup>11,12</sup>).

Ocean currents through key gateways into the Arctic Mediterranean have been measured since the late 1990s (ref. <sup>19</sup>). A recent compilation of volume transport measurements demonstrates that the exchange flow across the GSR has remained constant or slightly increased (the increase is not statistically significant)<sup>20</sup>. This indicates that the strength of the northern component of the AMOC has been stable over the past two decades. By contrast, measurements from a mooring array at  $26.5^\circ \text{N}$  in the North Atlantic indicate that the AMOC has been in a reduced state since 2008 (ref. <sup>21</sup>). This disconnect between a stable AMOC across the GSR and a weakened AMOC at  $26.5^\circ \text{N}$  is presently not well understood<sup>7,22–24</sup>.

Even though long-term volume transport measurements exist, robust estimates of ocean heat transport into the Arctic Mediterranean have yet to be determined. The ocean heat transport is a product of the temperature difference between compensating inflows and outflows and their volume transports. The greatest impediment for such a calculation is the requirement of a mass-balanced ocean circulation across the boundary of the Arctic Mediterranean<sup>25</sup>. Although published long-term observation-based volume transports conserve mass within uncertainties<sup>20</sup>, observational time series can never fulfil the requirement of complete mass balance. From this we can only calculate approximate heat transport across the GSR of  $\sim 300 \text{ TW}$  with no information about its temporal variability<sup>26,27</sup>. Recently, however, such mass-balanced heat transport estimates across the gateways to the Arctic Ocean were obtained using an inverse box model to constrain the hydrographic and velocity measurements<sup>28–30</sup>. Here, we extend this calculation to include the Nordic Seas using the same method and the longer measurement time series across the GSR to quantify the ocean heat transport into the Arctic Mediterranean over the period 1993–2016.

## Mass-balanced ocean circulation

To quantify the ocean circulation across the gateways of the Arctic Mediterranean, we consider published volume transport time series of 11 major ocean currents (Fig. 1). Following previous work<sup>20,26,27</sup>, the currents are divided into three distinct water mass groups: AW, OW

<sup>1</sup>Geophysical Institute, University of Bergen and Bjerknes Centre for Climate Research, Bergen, Norway. <sup>2</sup>Faroe Marine Research Institute, Tórshavn, Faroe Islands. <sup>3</sup>NORCE Norwegian Research Centre, Bergen, Norway. <sup>4</sup>Scottish Association for Marine Science, Oban, UK. <sup>5</sup>University of Akureyri, Akureyri, Iceland. <sup>6</sup>Marine and Freshwater Research Institute, Reykjavík, Iceland. ✉e-mail: [takamasa.tsubouchi@uib.no](mailto:takamasa.tsubouchi@uib.no)

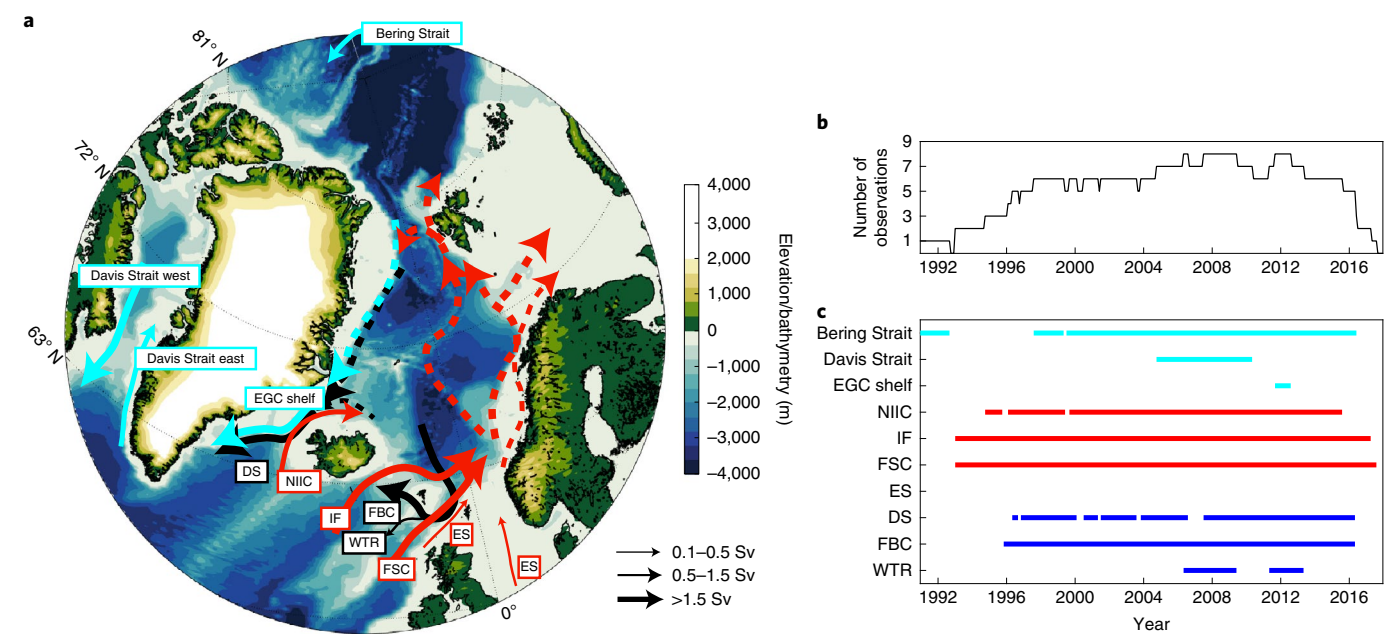


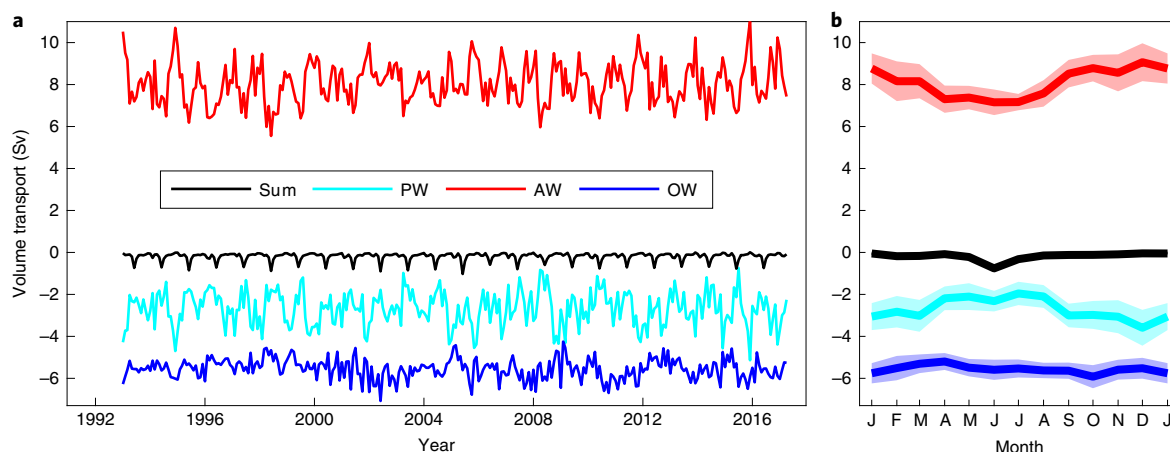
**Fig. 1 | Major ocean currents of the region and data coverage.** **a**, Schematic diagram of the major currents crossing the boundary of the Arctic Mediterranean. The currents are colour-coded according to their water mass category: cyan for PW, red for AW and black for OW. Only the currents included in the inverse calculation are labelled. The sizes of the arrows reflect the magnitude of the volume transports. **b**, The number of time series included in the inversion. **c**, Data coverage of each current included in the inversion.

and polar water (PW). AW is the warm and saline subtropical-origin water that flows northward across the GSR. The AW inflow into the Arctic Mediterranean takes place primarily within the Iceland–Faroe (IF)<sup>15</sup> and the Faroe–Shetland Channel (FSC)<sup>31</sup> branches between Iceland and Scotland, with some contributions also from the North Icelandic Irminger Current (NIIC)<sup>32</sup> west of Iceland and the European Shelf (ES)<sup>20</sup> branch which is a combination of flows over the Scottish shelf and through the English Channel. OW is the cold and dense water, commonly defined by a potential density greater than  $\sigma_\theta = 27.8 \text{ kg m}^{-3}$ , that returns southward through gaps in the GSR as dense plumes. The major OW plumes pass through Denmark Strait (DS)<sup>33</sup> and Faroe Bank Channel (FBC)<sup>22</sup>, with a minor contribution from Wyville Thomson Ridge (WTR)<sup>34</sup>. The dense water transport across the Iceland–Faroe Ridge is probably negligible<sup>35</sup> and has been disregarded. PW is a cold and fresh water mass primarily originating in the Arctic Ocean that flows southward on both sides of Greenland, through Davis Strait as the Baffin Island Current (here referred to as Davis Strait west)<sup>36</sup> and through Denmark Strait as the light portion of the East Greenland Current (here referred to as EGC shelf)<sup>37</sup>. Within the PW category, water is also imported into the Arctic Mediterranean through Bering Strait<sup>38</sup> and along the eastern side of Davis Strait (here referred to as Davis Strait east)<sup>36</sup>. While these inflows into the Arctic Mediterranean are not as cold and fresh as the PW emerging directly from the Arctic Ocean, they have densities below  $\sigma_\theta = 27.7 \text{ kg m}^{-3}$  and belong within the PW category<sup>39</sup>.

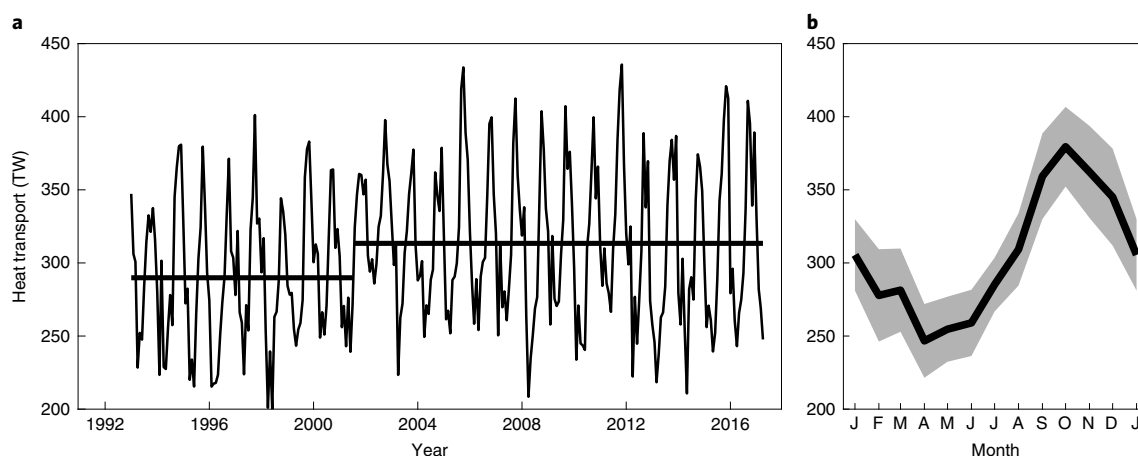
The time series of volume transport were combined using a box inverse model, a widely used method to quantify large-scale ocean circulation originally developed to resolve the classical oceanographic problem of reference level velocity<sup>40</sup>. We applied mass conservation as a constraint to obtain monthly mass-balanced ocean transports across the boundary of the Arctic Mediterranean (Supplementary Fig. 1). Each current was prescribed an a priori uncertainty (Supplementary Table 1). At each time step, the inverse calculation then optimally adjusted the transport of each current within the uncertainty bounds to obtain mass balance. Most of the

Table 1   Means, uncertainties and standard deviations of volume transports, heat transports and temperature transports based on the monthly mass-balanced ocean circulation between January 1993 and April 2017				
	Volume transports (Sv)		Heat/temperature transports (TW/TW-eq)	
	Mean ± uncertainty	±s.d.	Mean ± uncertainty	±s.d.
Water mass groups				
PW	−2.7 ± 1.3	±0.8	28 ± 8	±14
AW	8.0 ± 0.7	±1.0	273 ± 24	±41
OW	−5.6 ± 0.4	±0.5	4 ± 0.4	±2
Net boundary transports				
Ocean	−0.2 ± 1.5	±0.2	<b>305 ± 26</b>	<b>±51</b>
Sea ice	−0.01 ± 0.02	±0.02	<b>5 ± 0.1</b>	<b>±6</b>
Ocean plus sea ice	−0.2 ± 1.5	±0.2	<b>310 ± 26</b>	<b>±51</b>
AW components				
NIIC	0.9 ± 0.1	±0.3	24 ± 3	±11
IF	3.8 ± 0.4	±0.5	124 ± 13	±20
FSC	2.7 ± 0.4	±1.0	100 ± 15	±36
ES	0.6 ± 0.3	±0.1	25 ± 14	±4
The transport estimates are categorized into water mass groups, net boundary transports and AW components. Heat transports are in bold and are independent of a reference temperature. Temperature transports are calculated with reference to 0.0 °C.				

modifications (58%) were applied to the PW, which has a larger uncertainty, in particular the sparsely sampled EGC shelf (Fig. 1c). The modifications of the volume transport are expressed primarily in the month-to-month variability and in the seasonal cycle, while the long-term mean value is largely unchanged (Supplementary



**Fig. 2 | Mass-balanced volume transport across the boundary of the Arctic Mediterranean. a**, Monthly time series between January 1993 and April 2017. The time series are colour-coded according to their water mass category. **b**, Seasonalities (months J, January to D, December) and standard deviations of the time series.



**Fig. 3 | Mass-balanced ocean heat transport across the boundary of the Arctic Mediterranean. a**, Monthly time series between January 1993 and April 2017. The thick black line is a filtered time series using a 61-month Hanning filter. The horizontal lines represent the means of the two periods (1993–2000 and 2002–2016) defined by the change point analysis. **b**, Seasonality and standard deviation of the time series.

Fig. 2). The validity of our 23-yr inversion was assessed by comparing the entire 1993–2016 period (Table 1) to the well-sampled period of 2005–2012 (Supplementary Table 2). The statistics of the two periods are in excellent agreement, which lends confidence to our long-term inversion. Details of the inverse calculation and time series preparation are provided in Methods section.

The mass-balanced circulation obtained from the inversion is in good agreement with the in situ measurements in terms of means and variability on seasonal and longer time scales (Table 1 and Fig. 2)<sup>20</sup>. Over the entire 1993–2016 period the AW and OW volume transports were stable, apart from an increase of  $\sim 0.5$  Sv ( $1 \text{ Sv} = 10^6 \text{ m}^3 \text{ s}^{-1}$ ) between 1998 and 2002 (Supplementary Fig. 3). The AW volume transport is highest in winter and lowest in summer with a seasonal range of  $\sim 1.5$  Sv, while the OW volume transport does not have a clear seasonality (Fig. 2b).

### Ocean heat transport

Combining the mass-balanced circulation and the transport-weighted temperatures for each current, we have robustly quantified the ocean heat transport into the Arctic Mediterranean (Table 1 and Fig. 3a). The monthly ocean heat transport time series has

a large variability ranging from 200 to 450 TW, with a long-term mean of  $305 \pm 26$  TW. Details of the heat transport calculation and uncertainty estimates are provided in Methods section. The heat transport has a distinct seasonal cycle, with maximum in September–December and minimum in April–June, and an amplitude of about 120 TW (Fig. 3b). The seasonality is the combined result of a temperature-driven component (with maximum in July–November) and a velocity-driven component (which peaks in October–January; Supplementary Fig. 4). Considering only the temperature transport across the GSR, we obtain a value of  $281 \pm 24$  TW-equivalent (TW-eq). (Mass conservation is not ensured when considering individual branches of the circulation, hence we use a different terminology and unit, such as temperature transport and TW-eq; refs. <sup>29,41</sup>.) The temperature transport is in good agreement with a recent estimate of  $273 \pm 27$  TW based on repeat shipboard velocity and temperature measurements along the GSR during 2009–2016 (ref. <sup>8</sup>).

A key feature of the ocean heat transport time series is the substantial increase that took place during 1998–2002, which is particularly evident in the filtered time series (Fig. 3a). A change point detection method<sup>42</sup> identified a discontinuity in the monthly ocean

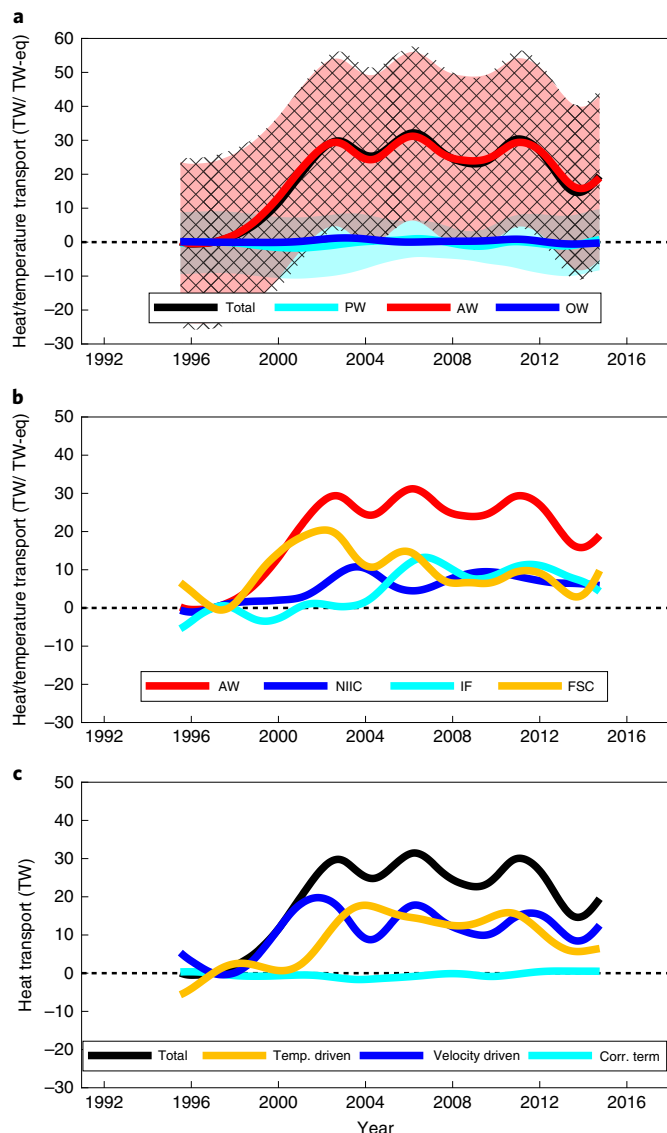


**Fig. 4 | Filtered ocean heat and temperature transport changes referenced to January 1997. a,** Changes in ocean heat transports (TW) in black and temperature transports of the distinct water masses (TW-eq) in colours. The shading represents uncertainty estimates. The time series are filtered using a 61-month Hanning filter. **b,** Contributions to the heat transport change by the temperature transport changes of three AW branches. **c,** Dominant causes of the heat transport change (Temp., temperature; Corr., correlation).

heat transport time series in July 2001 at the 99.9% confidence level. Compared to the 1993–2000 average, an additional 21 TW of heat was imported during 2002–2016, which is equivalent to a  $1.5 \text{ W m}^{-2}$  extra heat flux across the entire Arctic Mediterranean. The difference in ocean heat transport between the two periods is statistically significant at the 99.9% confidence level estimated using Welch's *t*-test as well as a bootstrap method<sup>43</sup>. To understand the cause of the increase, we decomposed the ocean heat transport time series into each water mass group (Fig. 4a). The increase stems in full from the AW contribution. Further decomposition into the different AW branches reveals that all three currents contributed to the increase at different times (Fig. 4b). We do not consider the ES branch here due to its low transport and the lack of long-term measurements. The temperature transport of the FSC increased first during 1998–2002,

followed by the NIIC around 2003 and the IF during 2004–2007. Relative to 1997, all three branches had 6–7 TW-eq higher temperature transports in 2012–2014. Although such a decomposition into different water mass groups and currents no longer ensures mass conservation, the same conclusion can be drawn using a constant reference temperature near the freezing point of  $-1.8^\circ\text{C}$  (Supplementary Fig. 5). While the increased temperature transports in the NIIC<sup>32</sup> and the IF<sup>15</sup> have been documented, the present study quantifies their relative contributions to the total ocean heat transport. Further decomposition sheds light on the dominant causes of the heat transport variability (Fig. 4c). Both temperature- and velocity-driven components contributed to the increased heat transport. The velocity-driven component increased first and is a reflection of increased AW and OW flow across the GSR during 1998–2002 (Supplementary Fig. 3), followed by an increase in the temperature-driven component during 2000–2004.

### Overturning in the Nordic Seas

Using a similar box inverse technique the ocean and sea ice heat transports across the gateways of the Arctic Ocean for the period 2004–2010 were recently quantified as  $180 \pm 23 \text{ TW}$  (refs. <sup>29,30</sup>). If we consider the same period of time and subtract this value from the heat transports into the entire Arctic Mediterranean, we obtain  $137 \pm 34 \text{ TW}$  for the Nordic Seas alone (Fig. 5). This is in good agreement with a comprehensive heat budget in the Nordic Seas of  $124 \text{ TW}$  based on hydrographic measurements during 1990–1999 (ref. <sup>44</sup>). Ocean heat transport into the Barents Sea was estimated as  $73 \text{ TW}$  for the period 1997–2007 (ref. <sup>45</sup>).

The water mass transformation from AW to OW that happens in the Arctic Mediterranean requires  $189 \pm 14 \text{ TW}$  of heat loss considering a temperature difference of  $8.4^\circ\text{C}$  and an OW volume transport of  $5.5 \pm 0.3 \text{ Sv}$ . If we assume that all of the heat loss from the Nordic Seas is used to form OW, the  $137 \pm 34 \text{ TW}$  of ocean heat transport sustains an overturning circulation in the Nordic Seas of  $4.0 \pm 0.7 \text{ Sv}$ . This implies that the remainder of the overturning,  $1.5 \pm 0.8 \text{ Sv}$ , takes place in the Arctic Ocean, primarily in the Barents Sea<sup>5</sup>. This estimate agrees well with other inverse calculations which estimate a  $1.3 \pm 0.7 \text{ Sv}$  production of Arctic Intermediate Water in the Barents Sea<sup>46</sup> and a net outflow of  $1.5 \text{ Sv}$  through Fram Strait<sup>29</sup>, most of which contributes to the Denmark Strait OW plume<sup>39,47</sup>. These results further emphasize the importance of water mass transformation in the Nordic Seas as a source of dense water to the lower limb of the AMOC<sup>7,8</sup>.

### Wider implications

Since 2000, heat has accumulated at a rate of  $\sim 1 \text{ W m}^{-2}$  or  $12 \text{ TW}$  in total in the ocean north of  $70^\circ\text{N}$  which includes about half of the Nordic Seas and the entire Arctic Ocean<sup>11,12</sup>. While this warming is reflected in substantial sea ice loss and a more pronounced AW influence at high latitudes<sup>11,12,16–18</sup>, the heat content of the Norwegian Sea has increased at an even higher rate<sup>9,10</sup>. Recent numerical and observational studies demonstrate that both surface heat flux and ocean heat transport into the Norwegian Sea regulate the heat content variability on interannual to decadal time scales<sup>10,48,49</sup>. The increase in ocean heat transport across the GSR of  $21 \text{ TW}$  that took place after 2001 is sufficient to account for most, if not all, of the heat accumulation in the Arctic Mediterranean. This emphasizes the crucial role of ocean heat transport in the high-latitudes climate system.

The AMOC transports warm water northward in the Atlantic Ocean and is a crucial component of the climate system<sup>1</sup>. In a warming climate, the AMOC is expected to weaken<sup>50</sup>. Measurements from a mooring array at  $26.5^\circ\text{N}$  indicate that the AMOC has been in a reduced state since 2008<sup>21</sup>. By contrast, the exchange flow of AW and OW across the GSR has been stable or slightly increased since 1992 (refs. <sup>20,22,33</sup>), and our results demonstrate that also the



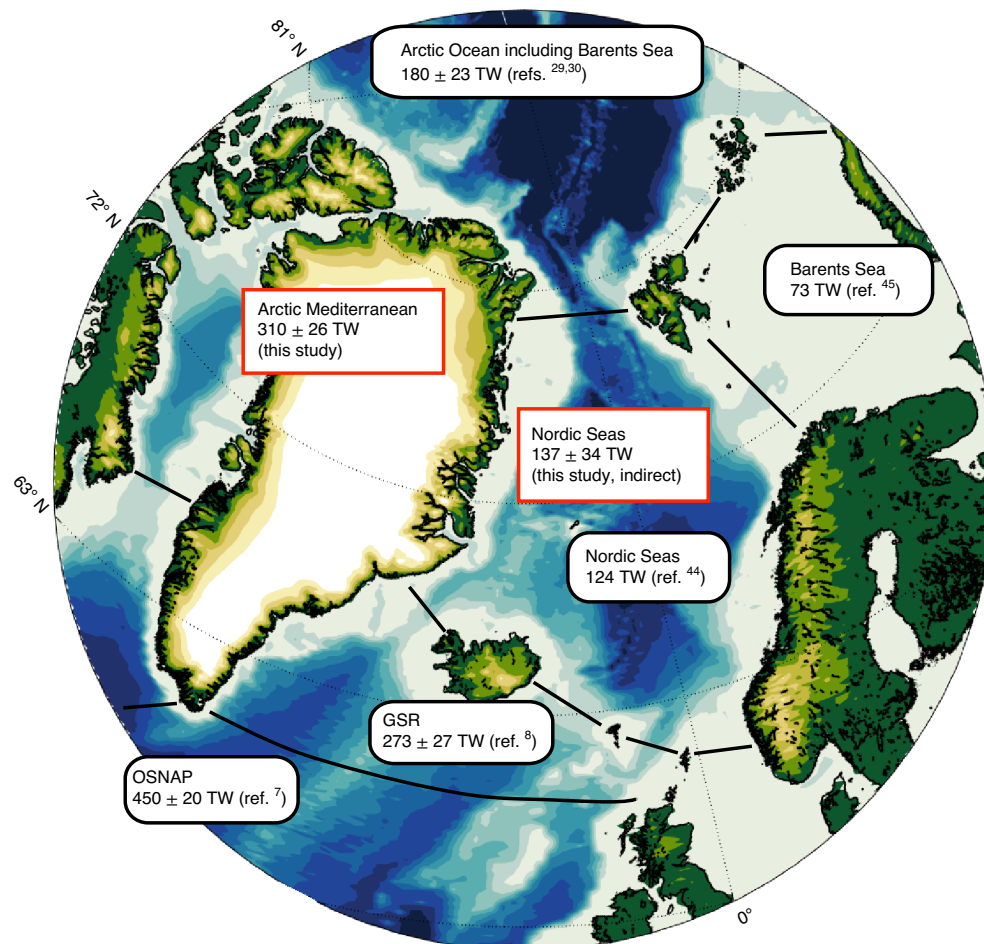


**Fig. 5 | Summary of ocean and sea ice heat transport estimates in the North Atlantic and Arctic Mediterranean.** The ocean and sea ice heat transports into the Arctic Mediterranean during 1993–2016 and the Nordic Seas during 2004–2010 obtained in this study are printed in the rectangular red boxes. The black ellipses show mass-balanced ocean and sea ice heat transports across a section (Overturning in the Subpolar North Atlantic Program (OSNAP), GSR) or into enclosed regions (Nordic Seas, Barents Sea and Arctic Ocean) from the recent literature for comparison and context.

ocean heat transport across the ridge has increased. This apparent disconnect between a stable overturning at high latitudes and a weakened circulation at mid-latitudes in the Atlantic Ocean is not well understood, but of key importance for accurate predictions of future climate states<sup>7,22–24</sup>.

### Online content

Any methods, additional references, Nature Research reporting summaries, source data, extended data, supplementary information, acknowledgements, peer review information; details of author contributions and competing interests; and statements of data and code availability are available at <https://doi.org/10.1038/s41558-020-00941-3>.

Received: 24 September 2019; Accepted: 24 September 2020;  
Published online: 23 November 2020

### References

- Buckley, M. W. & Marshall, J. Observations, inferences, and mechanisms of the Atlantic meridional overturning circulation: a review. *Rev. Geophys.* **54**, 5–63 (2016).
- Eldevik, T. et al. A brief history of climate—the northern seas from the Last Glacial Maximum to global warming. *Quat. Sci. Rev.* **106**, 225–246 (2014).
- Årthun, M., Kolstad, E., Eldevik, T. & Keenlyside, N. S. Time scales and sources of European temperature variability. *Geophys. Res. Lett.* **45**, 3597–3604 (2018).
- Mauritzen, C. Production of dense overflow waters feeding the North Atlantic across the Greenland–Scotland Ridge. Part 1. Evidence for a revised circulation scheme. *Deep Sea Res.* **43**, 769–806 (1996).
- Smedsrud, L. H. et al. The role of the Barents Sea in the Arctic climate system. *Rev. Geophys.* **51**, 415–449 (2013).
- Aagaard, K., Swift, J. H. & Carmack, E. C. Thermohaline circulation in the Arctic Mediterranean seas. *J. Geophys. Res.* **90**, 4833–4846 (1985).
- Lozier, M. S. et al. A sea change in our view of overturning in the subpolar North Atlantic. *Science* **363**, 516–521 (2019).
- Chafik, L. & Rossby, T. Heat, and freshwater divergences in the subpolar North Atlantic suggest the Nordic Seas as key to the state of the meridional overturning circulation. *Geophys. Res. Lett.* **46**, 4799–4808 (2019).
- Skagseth, Ø. & Mork, K. A. Heat content in the Norwegian Sea, 1995–2010. *ICES J. Mar. Sci.* **69**, 826–832 (2012).
- Mork, K. A., Skagseth, Ø. & Soiland, H. Recent warming and freshening of the Norwegian Sea observed by Argo data. *J. Clim.* **32**, 3695–3705 (2019).
- Mayer, M., Haimberger, L., Pietschnig, M. & Storto, A. Facets of Arctic energy accumulation based on observations and reanalyses 2000–2015. *Geophys. Res. Lett.* **43**, 10420–10429 (2016).
- Mayer, M. et al. An improved estimate of the coupled Arctic energy budget. *J. Clim.* **32**, 7915–7934 (2019).
- Holliday, N. P. et al. Reversal of the 1960s to 1990s freshening trend in the northeast North Atlantic and Nordic Seas. *Geophys. Res. Lett.* <https://doi.org/10.1029/2007gl032675> (2008).
- González-Pola, C., Larsen, K. M. H., Fratantoni, P. & Beszczynska-Möller, A. (eds) *ICES Report on Ocean Climate 2017* (ICES, 2018); <https://doi.org/10.17895/ices.pub.4625>
- Hansen, B. et al. Transport of volume, heat, and salt towards the Arctic in the Faroe Current 1993–2013. *Ocean Sci.* **11**, 743–757 (2015).

16. Polyakov, I. V. et al. Greater role for Atlantic inflows on sea-ice loss in the Eurasian basin of the Arctic ocean. *Science* **356**, 285–291 (2017).
17. Lind, S., Ingvaldsen, R. B. & Furevik, T. Arctic warming hotspot in the northern Barents Sea linked to declining sea-ice import. *Nat. Clim. Change* **8**, 634–639 (2018).
18. Perez-Hernandez, M. D. et al. Structure, transport, and seasonality of the Atlantic water boundary current north of Svalbard: results from a yearlong mooring array. *J. Geophys. Res.* **124**, 1679–1698 (2019).
19. Dickson, R., Meincke, J. & Rhines, P. (eds) *Arctic–Subarctic Ocean Fluxes: Defining the Role of the Northern Seas in Climate* (Springer, 2008).
20. Østerhus, S. et al. Arctic Mediterranean exchanges: a consistent volume budget and trends in transports from two decades of observations. *Ocean Sci.* **15**, 379–399 (2019).
21. Smeed, D. A. et al. The North Atlantic Ocean is in a state of reduced overturning. *Geophys. Res. Lett.* **45**, 1527–1533 (2018).
22. Hansen, B., Larsen, K. M. H., Hátun, H. & Østerhus, S. A stable Faroe Bank Channel overflow 1995–2015. *Ocean Sci.* **12**, 1205–1220 (2016).
23. Lozier, M. S., Roussinov, V., Reed, M. S. C. & Williams, R. G. Opposing decadal changes for the North Atlantic meridional overturning circulation. *Nat. Geosci.* **3**, 728–734 (2010).
24. Årthun, M., Eldevik, T. & Smedsrud, L. H. The role of Atlantic heat transport in future Arctic winter sea ice loss. *J. Clim.* **32**, 3327–3341 (2019).
25. Schauer, U. & Beszczynska-Möller, A. Problems with estimation and interpretation of oceanic heat transport—conceptual remarks for the case of Fram Strait in the Arctic Ocean. *Ocean Sci.* **5**, 487–494 (2009).
26. Hansen, B. et al. in *Arctic–Subarctic Ocean Fluxes: Defining the Role of the Northern Seas in Climate* (eds Dickson, R. R. et al.) 15–43 (Springer, 2008).
27. Eldevik, T. & Nilsen, J. E. O. The Arctic–Atlantic thermohaline circulation. *J. Clim.* **26**, 8698–8705 (2013).
28. Tsubouchi, T. et al. The Arctic Ocean in summer: a quasi-synoptic inverse estimate of boundary fluxes and water mass transformation. *J. Geophys. Res.* <https://doi.org/10.1029/2011jc007174> (2012).
29. Tsubouchi, T. et al. The Arctic Ocean seasonal cycles of heat and freshwater fluxes: observation-based inverse estimates. *J. Phys. Oceanogr.* **48**, 2029–2055 (2018).
30. Tsubouchi, T. et al. The Arctic Ocean volume, heat and fresh water transports time series from October 2004 to May 2010. *PANGAEA* <https://doi.org/10.1594/PANGAEA.909966> (2019).
31. Berx, B. et al. Combining in situ measurements and altimetry to estimate volume, heat and salt transport variability through the Faroe–Shetland Channel. *Ocean Sci.* **9**, 639–654 (2013).
32. Jónsson, S. & Valdimarsson, H. Water mass transport variability to the North Icelandic shelf, 1994–2010. *ICES J. Mar. Sci.* **69**, 809–815 (2012).
33. Jochumsen, K. et al. Revised transport estimates of the Denmark Strait overflow. *J. Geophys. Res.* **122**, 3434–3450 (2017).
34. Sherwin, T. J., Griffiths, C. R., Inall, M. E. & Turrell, W. R. Quantifying the overflow across the Wyville Thomson Ridge into the Rockall Trough. *Deep Sea Res.* **55**, 396–404 (2008).
35. Hansen, B. et al. Overflow of cold water across the Iceland–Faroe Ridge through the Western Valley. *Ocean Sci.* **14**, 871–885 (2018).
36. Curry, B., Lee, C. M., Petrie, B., Moritz, R. E. & Kwok, R. Multiyear volume, liquid freshwater, and sea ice transports through Davis Strait, 2004–10. *J. Phys. Oceanogr.* **44**, 1244–1266 (2014).
37. de Steur, L. et al. Liquid freshwater transport estimates from the East Greenland Current based on continuous measurements north of Denmark Strait. *J. Geophys. Res.* **122**, 93–109 (2017).
38. Woodgate, R. A. Increases in the Pacific inflow to the Arctic from 1990 to 2015, and insights into seasonal trends and driving mechanisms from year-round Bering Strait mooring data. *Prog. Oceanogr.* **160**, 124–154 (2018).
39. Rudels, B. et al. The interaction between waters from the Arctic Ocean and the Nordic Seas north of Fram Strait and along the East Greenland Current: results from the Arctic Ocean-02 Oden expedition. *J. Mar. Sys.* **55**, 1–30 (2005).
40. Wunsch, C. *The Ocean Circulation Inverse Problem* (Cambridge Univ. Press, 1996).
41. Talley, L. D. Shallow, intermediate, and deep overturning components of the global heat budget. *J. Phys. Oceanogr.* **33**, 530–560 (2003).
42. Lanzante, J. R. Resistant, robust and non-parametric techniques for the analysis of climate data: theory and examples, including applications to historical radiosonde station data. *Int. J. Climatol.* **16**, 1197–1226 (1996).
43. Emery, W. J. & Thomson, R. E. *Data Analysis Methods in Physical Oceanography* (Elsevier Science, 2014).
44. Segtnan, O. H., Furevik, T. & Jenkins, A. D. Heat and freshwater budgets of the Nordic seas computed from atmospheric reanalysis and ocean observations. *J. Geophys. Res.* <https://doi.org/10.1029/2011jc006939> (2011).
45. Smedsrud, L. H., Ingvaldsen, R., Nilsen, J. E. O. & Skagseth, Ø. Heat in the Barents Sea: transport, storage, and surface fluxes. *Ocean Sci.* **6**, 219–234 (2010).
46. Mauritzen, C. Production of dense overflow waters feeding the North Atlantic across the Greenland–Scotland Ridge. Part 2. An inverse model. *Deep Sea Res.* **43**, 807–835 (1996).
47. Håvik, L. et al. Evolution of the east Greenland current from Fram Strait to Denmark Strait: synoptic measurements from summer 2012. *J. Geophys. Res.* **122**, 1974–1994 (2017).
48. Årthun, M. & Eldevik, T. On anomalous ocean heat transport toward the Arctic and associated climate predictability. *J. Clim.* **29**, 689–704 (2016).
49. Asbjørnsen, H., Årthun, M., Skagseth, Ø. & Eldevik, T. Mechanisms of ocean heat anomalies in the Norwegian Sea. *J. Geophys. Res.* <https://doi.org/10.1029/2018JC014649> (2019).
50. IPCC *Climate Change 2013: The Physical Science Basis* (eds Stocker, T. F. et al.) (Cambridge Univ. Press, 2013).

**Publisher's note** Springer Nature remains neutral with regard to jurisdictional claims in published maps and institutional affiliations.

© The Author(s), under exclusive licence to Springer Nature Limited 2020

## Methods

**Data.** To derive a mass-balanced ocean circulation across the boundary of the Arctic Mediterranean, we consider the full mass budget of the Arctic Mediterranean. The mass budget can be expressed in the form

$$\frac{\partial M}{\partial t} = F_{ma}^o + F_{ma}^i + F_{ma}^{surf} \quad (1)$$

where  $\frac{\partial M}{\partial t}$  is the change in interior mass storage with time (storage flux),  $F_{ma}^o$  and  $F_{ma}^i$  are the horizontal exchanges of mass due to ocean circulation and sea ice export across the side boundary, and  $F_{ma}^{surf}$  is the addition or removal of mass due to surface freshwater fluxes. These freshwater fluxes are net precipitation minus evaporation (P–E), river runoff, and Greenland ice sheet and land ice melt. We consider  $\frac{\partial M}{\partial t}$  and  $F_{ma}^{surf}$  together in the inversion because this combined term is balanced by horizontal exchange of mass due to ocean circulation and sea ice export.

For  $F_{ma}^o$ , we consider published volume transport records of the exchanges across the boundary of the Arctic Mediterranean that cover different time periods between 1993 and 2016 (Fig. 1c). They are categorized into three distinct water mass groups: PW, AW and OW. For the PW, we use observations from Bering Strait for the period 1992–2016 (ref. <sup>30</sup>) and from the EGC shelf during 2011–2012 (ref. <sup>37</sup>). For the AW, we use transport estimates of IF<sup>15</sup> and FSC<sup>31</sup> branches during 1993–2017 and NIIC during 1994–2015 (ref. <sup>32</sup>). For the OW, we use observations from DS<sup>33</sup> and FBC<sup>22</sup> during 1996–2016 and from WTR during 2006–2009 and 2011–2013 (ref. <sup>34</sup>). Some of the minor inflows and outflows lack sustained observations. For the ES branch, we prescribe a constant AW inflow of 0.6 Sv with a seasonal cycle of amplitude 0.1 Sv (ref. <sup>20</sup>). In Davis Strait, we distinguish the southward Baffin Island Current on the western side and the northward West Greenland and West Greenland Slope Currents on the eastern side<sup>36</sup> using a separation longitude of 58°W (ref. <sup>28</sup>) based on monthly velocity fields during 2004–2010 (ref. <sup>30</sup>).

The  $F_{ma}^i$  is quantified using monthly effective sea ice thickness and velocity data from the Pan-Arctic Ice Ocean Modelling and Assimilation System (PIOMAS) v2.1 (ref. <sup>31</sup>). The effective sea ice thickness is a product of sea ice thickness and sea ice concentration. The PIOMAS product covers the entire period of the inversion.

The  $F_{ma}^{surf}$  is prescribed on the basis of the mean seasonal cycle of the surface freshwater flux estimate to the Arctic Ocean<sup>32</sup> and the mean seasonal cycle of P–E to the Nordic Seas on the basis of ERA-Interim<sup>33</sup>. Greenland ice sheet and land ice melt contributions<sup>34</sup> are an order of magnitude smaller than other freshwater fluxes and have been neglected. The  $\frac{\partial M}{\partial t}$  is prescribed with a satellite-derived storage flux in the central Arctic Ocean during 2003–2014 (ref. <sup>35</sup>) assuming a spatially uniform sea-level change<sup>36</sup>. Here we use the spatial average values of  $F_{ma}^{surf}$  and  $\frac{\partial M}{\partial t}$  across the Arctic Mediterranean and consider only its mean seasonal cycle. We do not take interannual variability into account since the uncertainty of  $F_{ma}^{surf}$  is high<sup>37</sup>. The combined surface freshwater flux and storage flux ( $F_{ma}^{surf} - \frac{\partial M}{\partial t}$ ) has an annual mean value of 196 mSv with a pronounced seasonal cycle which peaks in June at ~650 mSv, and it is reduced to 80–250 mSv during the rest of the year. A sensitivity test of the inverse model with constant ( $F_{ma}^{surf} - \frac{\partial M}{\partial t}$ ) over the entire period confirms that temporal variability of this term has negligible impact (<0.1%) on the resulting mass-balanced ocean circulation and ocean heat transport.

**Short time series and data gaps.** Our inverse calculation extends from January 1993 to April 2017, coincident with volume transport records from the two major AW inflow branches (IF and FSC; Fig. 1c). These are the most critical measurements, as the bulk of the ocean heat transport variability originates in these AW branches (Table 1 and Fig. 4b). While measurements of the major AW and OW branches cover the period 1996–2016, some of the ocean transport records are shorter than the period of inversion, in particular some of the PW branches. The records occasionally also contain data gaps. These have various origins, such as data outliers or missing instruments. To obtain continuous monthly transport time series over the entire period, gaps shorter than 3 months duration are filled by linear interpolation, whilst gaps exceeding 3 months are filled using the mean seasonal cycle from the record. Short time series were extended using the average value of the record modulated by its mean seasonal cycle. These extended time series are assigned a greater uncertainty as described in the following section.

**Box inverse model settings.** We apply four mass constraints to the box inverse model, which arise from conserving mass in each of the three water mass groups (PW, AW and OW) as well as the total mass. The model considers four different mechanisms to satisfy the full mass constraint (equation (1)). These are horizontal exchange of water due to ocean circulation ( $F_{ma}^o$ ) and sea ice ( $F_{ma}^i$ ), combined effect of net surface freshwater fluxes minus interior mass storage change ( $F_{ma}^{surf} - \frac{\partial M}{\partial t}$ ). Diapycnal exchanges of water from one water mass to another within the interior of the Arctic Mediterranean are also considered to satisfy the mass constraints for the three water mass groups. In practice, the four mass constraints are expressed by an equation,

$$Ab = d + \varepsilon \quad (2)$$

where  $m \times n$  matrix  $A$  contains information about the geometry of the system ( $m$  is the total number of constraints and  $n$  is the total number of unknowns). Vector  $b$  is

an  $n \times 1$  vector and contains sets of unknowns that the inversion solves. The  $m \times 1$  vector  $d$  contains information about the magnitudes of the initial imbalances for each constraint. The  $m \times 1$  vector  $\varepsilon$  is an error vector. Full details of the box inverse model are available in the Appendix of a paper which performed a similar inversion for the Arctic Ocean<sup>29</sup>.

The four mass constraints ( $m = 4$ ) are satisfied by modifying initial estimates of 25 unknown parameters ( $n = 25$ ), which consist of 11  $F_{ma}^o$  velocity parameters and 11  $F_{ma}^i$  velocity parameters for the 11 defined ocean currents, one ( $F_{ma}^{surf} - \frac{\partial M}{\partial t}$ ) velocity parameter and two diapycnal velocity parameters between water mass interfaces below and above the AW. The parameters are initialized as follows: first guesses for the  $F_{ma}^o$  velocity parameters are obtained from the monthly volume transports scaled by the corresponding cross-sectional areas. The  $F_{ma}^i$  velocity parameters are initialized using the PIOMAS sea ice volume transport time series. The ( $F_{ma}^{surf} - \frac{\partial M}{\partial t}$ ) velocity is initialized from the prescribed repeat seasonal cycle. The diapycnal velocities are set to zero. Note that salt is not constrained due to the substantial variability of PW salinity that we do not have sufficient observations to fully resolve. Unlike previous inverse model studies<sup>28,29</sup>, we compute only ocean heat transports due to the lack of salt constraints. While PW temperature measurements are also scarce, the variability in temperature is comparatively small and sensitivity experiments indicate that this has only a minor impact on our ocean heat transport estimate (2% at most).

Row and column weights are used to prescribe uncertainties for both the constraints and the unknown parameters. The uncertainties of the constraints are: 2.0 Sv for the PW layer, 1.0 Sv for the AW layer, 0.5 Sv for the OW layer and 0.01 Sv for the whole water column mass balance. For the  $F_{ma}^o$  velocities we apply the published uncertainty estimates listed in Supplementary Table 1. At times when volume transport estimates are not available, the uncertainty is doubled. For the  $F_{ma}^i$  and ( $F_{ma}^{surf} - \frac{\partial M}{\partial t}$ ) velocities the uncertainties are set to 30% and 100% of the initial estimates, respectively. For the diapycnal velocity, the uncertainty is set to  $10^{-4} \text{ m s}^{-1}$ .

The uncertainties of the  $F_{ma}^o$  (Supplementary Table 1) are key parameters to find the optimal inverse adjustment to achieve the mass balance. We rely on published uncertainty estimates with the exception of the EGC shelf branch. The reported error estimate is  $\pm 0.46 \text{ Sv}$  which stems from the gridding procedure alone<sup>37</sup>. This is probably an underestimate because the mooring array did not extend across the width of the Greenland shelf. We assign a higher uncertainty of  $\pm 1.0 \text{ Sv}$ , hence EGC shelf has the highest uncertainty among the 11 branches. With this uncertainty, 58% of the inverse model modifications in volume transport are applied to the PW layer. If we assign a lower uncertainty of  $\pm 0.5 \text{ Sv}$  to the EGC shelf transport, the inverse model modifications applied to the PW layer are reduced to 50%. This corresponds to a change in 1 TW in the 1993–2016 mean ocean heat transport, which is well below the total uncertainty of 26 TW and demonstrates that the inversion is not very sensitive to the high uncertainty of the EGC shelf transport.

**Box inverse model adjustments.** Supplementary Fig. 1 shows the net volume transport time series before and after the inversion. This net volume transport is balanced by other terms in the mass budget (equation (1)), such as the  $F_{ma}^i$  and ( $F_{ma}^{surf} - \frac{\partial M}{\partial t}$ ). Without adjustments, the mean imbalance is  $-0.3 \pm 1.4 \text{ Sv}$ . The month-to-month changes range from  $-4$  to  $+3 \text{ Sv}$ . It has a clear seasonality, with a net inflow in winter and a net outflow in summer because of the AW volume transport seasonality<sup>30</sup>. During the most data-rich period of 2004–2010 the imbalances were generally reduced. After the inversion the net volume transport becomes  $-0.2 \pm 0.2 \text{ Sv}$  with a distinct seasonal cycle that peaks in June. In June, a net outflow is largely balanced by the increased river runoff to the Arctic Ocean<sup>32</sup>.

We next examine how inverse modifications were introduced (Supplementary Fig. 2). The full depth inverse model modifications are  $0.1 \pm 1.3 \text{ Sv}$  (mean  $\pm$  s.d.). For that, the water mass inverse model modifications are  $0.0 \pm 0.7 \text{ Sv}$  in the PW layer,  $0.0 \pm 0.3 \text{ Sv}$  in the AW layer and  $0.0 \pm 0.2 \text{ Sv}$  in the OW layer. As mentioned in the previous paragraph, 58% of the inverse model modifications in volume transport are applied to the PW layer.

**Quantification of the ocean heat transport.** From the mass-balanced ocean circulation, the ocean heat transport  $F_H^o$  can be quantified as the product of the temperature difference between compensating inflows and outflows and their volume transports. In practice, the ocean heat transport is estimated as a summation of temperature transports for each branch  $j$ , such that

$$F_H^o = \sum_{j=1}^N \rho_o c_p^o V_j (\Theta_j - \Theta_{ref}) \quad (3)$$

where  $\rho_o$  is the density of sea water,  $c_p^o$  is the specific heat capacity of sea water,  $V_j$  is the volume transport estimate from the inverse model,  $\Theta_j$  is the transport-weighted potential temperature and  $\Theta_{ref}$  is a reference temperature here set to be  $0^\circ \text{C}$ . Note that we distinguish heat transport and temperature transport by terminology and units<sup>28,41</sup>. When the transport is sensitive to the choice of reference temperature, we refer to it as temperature transport with unit Watt-equivalent (W–eq). This is the case when the sum of all  $V_j$  is not zero, such as estimates from single gateways or water masses. The transport becomes almost independent from the choice of



reference temperature when mass is balanced (the sum of all  $V_j$  is zero), then we refer to it as heat transport with unit W.

As summarized in Supplementary Table 3, for five of the 11 branches the transport-weighted potential temperatures  $\Theta_j$  are calculated from published temperature transport measurements (Bering Strait<sup>38</sup>, Davis Strait west<sup>36</sup>, Davis Strait east<sup>36</sup>, NIIC<sup>32</sup> and IF<sup>15</sup>). For the remaining branches we use alternative information to represent the temperature variability. We use: (1) moored temperature time series for DS<sup>38</sup> and FBC<sup>22</sup>; (2) annual mean temperature variability observed at sustained long-term hydrographic transects<sup>14</sup> with repeat seasonal cycle for FSC and ES branches<sup>39</sup>; (3) fixed temperature for EGC shelf<sup>60</sup> and WTR<sup>34</sup> branches. For the FSC and ES branches, published annual mean Shetland shelf temperature (defined as temperature at salinity cores on the Shetland shelf)<sup>14</sup> is used, but for the FSC the annual mean temperature is lowered by 1 °C to represent the FSC temperature by considering the temperature and velocity distributions along the Fair Isle–Munken transect<sup>31</sup>. For the FSC and ES, seasonal cycles with amplitudes of 0.8 and 1.3 °C, respectively, that peak in September are prescribed on the basis of the observed upper ocean temperature variability along the section<sup>39</sup>.

**Error estimates.** After the inversion, a posteriori uncertainties are calculated as the square root of the diagonal component of the error covariance matrix<sup>28,40</sup>. Regarding the uncertainty of the long-term mean, we note that there are two different kinds of uncertainty: random and systematic<sup>61</sup>. Random uncertainty follows a probability distribution function and can be reduced by frequent sampling. Systematic uncertainty, on the other hand, is independent of the number of samples. We note that it is sometimes challenging to categorize the uncertainty into the two different types. Moreover, the sources of uncertainty are not always well documented in the literature. As such, we assume that the uncertainty is entirely systematic, which results in very conservative error estimates.

**Statistical significance of the heat transport increase.** The statistical significance of the difference in ocean heat transport between the 1993–2000 average and 2002–2016 average of 21 TW was evaluated using Welch's *t*-test and a bootstrap method<sup>43</sup>. For Welch's *t*-test, the statistic  $Z$  was calculated as follows:

$$Z = \frac{\bar{X}_1 - \bar{X}_2}{\sqrt{s_1^2/N_1 + s_2^2/N_2}} \quad (4)$$

where  $\bar{X}_j$ ,  $s_j$  and  $N_j$  are sample average, sample standard deviation and sample size, respectively, over the  $j$ th period. The statistical significance of the heat transport difference between the two periods was then evaluated using a two-tailed test and assuming a normal distribution ( $P=0.0006$ ). The statistical significance was also evaluated using the bootstrap method, which is a procedure that involves random sampling with replacement from the dataset and does not require any assumptions about the underlying probability distribution. The original time series were randomly shuffled to generate 10,000 pseudo time series to test the statistical significance ( $P=0.0007$ ). For both cases, the increase in ocean heat transport of 21 TW between the two periods was found to be statistically significant above the 99.9% confidence level.

**Decomposition of the ocean heat transport.** To investigate causes of variability, the ocean heat transport  $F_H^o\{V, \Theta\}$  is decomposed as follows:

$$F_H^o\{V, \Theta\} = F_H^o\{\bar{V}, \bar{\Theta}\} + F_H^o\{\bar{V}, \Theta'\} + F_H^o\{V', \bar{\Theta}\} + F_H^o\{V', \Theta'\} \quad (5)$$

where overbar indicates average over time and prime indicates deviation from the mean. Thus, the term  $F_H^o\{\bar{V}, \bar{\Theta}\}$  represents the 'mean-transport' component with no temporal variability, the term  $F_H^o\{\bar{V}, \Theta'\}$  is the 'temperature-driven' component resulting from temperature variability in each current,  $F_H^o\{V', \bar{\Theta}\}$  is the 'velocity-driven' component resulting from volume transport variability in each current and  $F_H^o\{V', \Theta'\}$  is the 'correlation term' resulting from the covariance of the two.

## Data availability

The mass-balanced ocean volume and heat transports are available at the Norwegian Marine Data Centre repository at <http://metadata.nmdc.no/metadata-api/landingpage/0a2ae0e42ef7af767a920811e83784b1>. The volume transport time series for GSR branches (IF, FSC, NIIC, DS and FBC) are available at Oceansites website <http://www.oceansites.org/tma/gsr.html>. The WTR data are available through <https://www.bodc.ac.uk>. The objectively mapped sections in Davis Strait are available via <http://iop.apl.washington.edu/data.html>. The Bering Strait data are available at project website <http://psc.apl.washington.edu/HLD/>

[Bstrait/bstrait.html](http://bstrait/bstrait.html). The Arctic Ocean heat transport estimates during 2004–2010 are available at <https://doi.org/10.1594/PANGAEA.909966>. The ERA-Interim reanalysis data were obtained from European Centre for Medium-Range Weather Forecasts (<https://www.ecmwf.int/en/forecasts/datasets/reanalysis-datasets/era-interim>). The PIOMAS were obtained from the Polar Science Centre at University of Washington (<http://psc.apl.uw.edu/research/projects/arctic-sea-ice-volume-anomaly/>).

## References

- Zhang, J. L. & Rothrock, D. A. Modeling global sea ice with a thickness and enthalpy distribution model in generalized curvilinear coordinates. *Monthly Weather Rev.* **131**, 845–861 (2003).
- Bacon, S., Aksentov, Y., Fawcett, S. & Madec, G. Arctic mass, freshwater and heat fluxes: methods and modelled seasonal variability. *Phil. Trans. R. Soc. A* <https://doi.org/10.1098/rsta.2014.0169> (2015).
- Dee, D. P. et al. The ERA-Interim reanalysis: configuration and performance of the data assimilation system. *Quart. J. R. Meteor. Soc.* **137**, 553–597 (2011).
- Shepherd, A. et al. Mass balance of the Greenland Ice Sheet from 1992 to 2018. *Nature* **579**, 233–239 (2020).
- Armitage, T. W. K. et al. Arctic sea surface height variability and change from satellite radar altimetry and GRACE, 2003–2014. *J. Geophys. Res.* **121**, 4303–4322 (2016).
- Fukumori, I., Wang, O., Llovel, W., Fenty, I. & Forget, G. A near-uniform fluctuation of ocean bottom pressure and sea level across the deep ocean basins of the Arctic Ocean and the Nordic Seas. *Prog. Oceanogr.* **134**, 152–172 (2015).
- Haine, T. W. N. et al. Arctic freshwater export: status, mechanisms, and prospects. *Glob. Planet. Change* **125**, 13–35 (2015).
- Jochumsen, K., Quadfasel, D., Valdimarsson, H. & Jónsson, S. Variability of the Denmark Strait overflow: moored time series from 1996–2011. *J. Geophys. Res.* <https://doi.org/10.1029/2012jc008244> (2012).
- Hátun, H., Sandø, A. B., Drange, H. & Bentsen, M. in *The Nordic Seas: An Integrated Perspective* (Drange, H. et al.) 239–250 (AGU, 2005).
- Harden, B. E. et al. Upstream sources of the Denmark Strait overflow: observations from a high-resolution mooring array. *Deep Sea Res.* **112**, 94–112 (2016).
- Evaluation of Measurement Data—Guide to the Expression of Uncertainty in Measurement*. Vol. 100 (JCCM, 2008).

## Acknowledgements

Support for this work was provided by the Trond Mohn Foundation under grant no. BFS2016REK01 (T.T. and K.V.), the European Union's FP7 grant no. 308299, NACLIM project (C.J.) and the European Union's Horizon 2020 research and innovation programme under grant no. 727852, Blue-Action project (B.H., K.M.H.L., S.Ø., S.J. and H.V.). We acknowledge R. Dickson's active role in initiating and promoting the integration of the Nordic Seas and Arctic Ocean boundary observation arrays over recent decades. The sustained mooring observations across GSR during 1993–2016 were funded through many national and international research projects including EU research projects such as VEINS (EU contract no. MAST-III MAS3960070), THOR (EU grant no. 212643) and NACLIM (EU grant no. 308299). Bering Strait data and analysis were supported by various NSF, NOAA and ONR grants, including NSF grant no. NFS-0856786 and the NOAA-RUSALCA programme. The Davis Strait programme was supported by the US National Science Foundation under grant nos. ARC0632231 and ARC1022472.

## Author contributions

T.T. and K.V. conceived and developed the study. T.T. integrated and analysed the data with inputs from all authors. T.T. and K.V. wrote the paper. All authors interpreted the results and clarified the implications.

## Competing interests

The authors declare no competing interests.

## Additional information

**Supplementary information** is available for this paper at <https://doi.org/10.1038/s41558-020-00941-3>.

**Correspondence and requests for materials** should be addressed to T.T.

**Peer review information** *Nature Climate Change* thanks Andrea Storto and Andrey Pnyushkov for their contribution to the peer review of this work.

**Reprints and permissions information** is available at [www.nature.com/reprints](http://www.nature.com/reprints).